Title

3-D Protoacoustic Imaging Through a Planar Ultrasound Array: A Simulation Workflow

Journal

IEEE Transactions on Radiation and Plasma Medical Sciences, 7(1)

ISSN

2469-7311

Authors

Samant, Pratik

Trevisi, Luis M

Chen, Yong

et al.

Publication Date

2023

DOI

10.1109/trpms.2022.3177236

Peer reviewed

Published in final edited form as:

IEEE Trans Radiat Plasma Med Sci. 2023 January ; 7(1): 83–95. doi:10.1109/trpms.2022.3177236.

3-D Protoacoustic Imaging Through a Planar Ultrasound Array: A Simulation Workflow

Pratik Samant[#],
Stephenson School of Biomedical Engineering, University of Oklahoma, Norman, 73071, USA and now is with the Department of Oncology, University of Oxford, and Oxford University Hospitals NHS Foundation Trust, Oxford, Oxfordshire, UK.

Luis M. Trevisi[#],
Chemical, Biological, & Materials Engineering, University of Oklahoma, Norman, 73071, USA.

Yong Chen,
Department of Radiation Oncology, University of Oklahoma Health Sciences Center, Oklahoma City, OK, USA.

Townsend Zwart,
Vice President of Advanced Development at Mevion Medical Systems, Littleton, MA, 01460, USA

Liangzhong Xiang
Departments of Biomedical Engineering and Radiology, University of California Irvine, Irvine, CA, USA, Department of Radiological Sciences, University of California, Irvine, CA, USA and Beckman Laser Institute & Medical Clinic, University of California, Irvine, Irvine, CA, USA.

[#] These authors contributed equally to this work.

Abstract

Bragg peak range uncertainties are a persistent constraint in proton therapy. Pulsed proton beams generate protoacoustic emissions proportional to absorbed proton energy, thereby encoding dosimetry information in a detectable acoustic wave. Here, we seek to derive and model 3D protoacoustic imaging with an ultrasound array and examine the frequency characteristics of protoacoustic emissions. A formalism is presented through which protoacoustic signals can be characterized considering transducer bandwidth as well as pulse duration of the incident beam. We have also collected an experimental proton beam intensity signal from a Mevion S250 clinical machine to analyze our formalism. We also show that proton-acoustic image reconstruction is possible even when the noise amplitude is larger than the signal amplitude on individual transducers. We find that a 4μs Gaussian proton pulse can generate a signal in the range of MHz as long as the spatial heating function has sufficiently high temperature gradients.

Corresponding author: Liangzhong Xiang (liangzhx@hs.uci.edu).

VI. CONFLICTS OF INTEREST STATEMENT

All authors declare that they have no known conflicts of interest in terms of competing financial interests or personal relationships that could have an influence or are relevant to the work reported in this paper.

Keywords

Radiation Therapy; Image guided therapy devices; Analytical; Analytical dosimetry; Image guided therapy

I. Introduction

Protons offer dominant advantages over photons for radiation therapy due to the unique depth-dose characteristics of protons (called Bragg Peak). In current proton therapy clinical procedure, Bragg peak localization is calculated using a planning CT, and then attempts are made to position the patient similarly to simulations. However, the steep dose gradient of the proton Bragg peak is not always used to its full extent in practice. This is because there is substantial uncertainty about the proton beam range, which carries the risk of overdosing healthy tissues or underdosing the target. The range uncertainty of proton beams has several sources, such as the non-uniqueness and inaccuracy of CT Hounsfield units to proton stopping power, CT imaging artefacts, and changes in the patient during treatment caused by mispositioning, breathing, etc. Therefore, accurate proton range verification remains an important clinical objective, ideally done through beam imaging and cross-correlation with known treatment plans.

Fortunately, pulsed proton beams generate dectectable acoustic emissions of proportional amplitude to the deposited dose [1]–[5]. This ‘protoacoustic’ phenomenon presents a unique oppurtunity for range verificiation as well as dose imaging, as the Bragg peak itself is a high dose area and therefore a strong protoacoustic emitter [6], [7]. This means that with the simple addition of an ultrasound transducer array (having appropriate frequency bandwidth), real-time proton dosimetry is possible *in vivo*. Such a set-up is illustrated in Figure 1. First, an incident pulsed proton beam hits the prostate region, thus inducing a protoacoustic emission, This protoacosutic emission can be detected by a transducer array (in our case, a 16 × 16 element square array with element dimensions 1.3 mm × 1.3 mm × 2.5 mm) placed close enough to the acoustic source. As long as the array can capture the acosutic signal with acceptable signal-to-noise ratio, the transducer can be used to reconsruct a 3D image of the relatve dose deposition of the beam.

In the context of protoacoustic research, there have been several simulation studies in the field examining different setups and problems. Recently, van Dongen *et al.* [8] constructed a 3D simulation in which model-based inversion was deployed to reconstruct 3D dose distributions from simulated noisy pressure fields, taking tissue heterogeneities into account.

However, delivery uncertainties (spot MU (monitor units), spot position and AA (adaptive aperture) positions) were not considered as the initial dose used was not calculated directly from the logfile of a clinical machine.

Assman *et al.* [3] were able to detect signals in 3D using a circular detector array scanned laterally, however in this setup lateral scanning is necessary and single shot 3D dose mapping is not possible. Ahmad *et al.* [1] used a simulated system to determine the detection threshold in protoacoustic simulations, but did not simulate imaging.

Jones *et al.* [9] and Yu *et al.* [10] performed detailed 2D simulations, but did not model full 3D propagation in their simulation studies nor used a x-ray linear accelerators (LINACs) log file for the initial pressure. Recently, protoacoustic signals have been experimentally detected by a single low frequency acoustic detector[1], [3], [4], the time of flight method was used to determine the actual travel time between the proton trigger signal and the measured acoustic wave. However, extensive benchmark work was needed to calibrate the measured acoustic travel distance with the clinical proton range (distal 90% of Bragg Peak). Therefore, to localize the Bragg peak of the proton beam, multiple acoustic detectors are needed.

In this manuscript we provide a simulation workflow that models 3D protoacoustic imaging through a detector array using a clinical machine's logfile to generate the initial pressure, thereby enabling planning of protoacoustic imaging experiments. We also analyze the frequency characteristics of the resultant protoacoustic signal. The main constraints in deploying a multi-detector system for imaging of the proton beam dose deposition is frequency of the acoustic signal. As higher frequencies are associated with higher resolution, protoacoustic imaging resolution is determined by the highest detectable frequency in the signal.

II. Materials and Methods

A. Theory of the Protoacoustic Effect

The protoacoustic effect is a thermoacoustic phenomenon, wherein incident pulsed proton radiation rapidly deposited energy inside the target tissue. This rapid deposition of energy results in a localized temperature gradient and subsequent thermoelastic expansion within the sample. As the target tissue expands, an acoustic wave is emitted, and propagates through the sample in three dimensions. A transducer array can then be placed near the source on the surface of the tissue to image proton energy deposition. Nevertheless, considerations about the exact position need to be carefully taken as the optimal position will prevent blocking the beam path while avoiding bone and air gaps between the source and the transducer.

The governing wave equation of the induced protoacoustic signal is as follows

$$\left(\nabla^2 - \frac{1}{v_s^2}\frac{\partial^2}{\partial t^2}\right)p(\boldsymbol{r},t) = -\frac{\beta}{\kappa v_s^2}\frac{\partial T(\boldsymbol{r},t)}{\partial t^2} \quad (1)$$

where v_s is the speed of sound, p is the protoacoustic pressure, $\boldsymbol{r}$ is the position vector, t is time, β is the thermal coefficient of volume expansion, κ is the isothermal compressibility, and T is the temperature.[11] This equation is commonly solved for a delta function excitation with a Green's function approach.[9], [11], [12] Extension of the solution to a pulse of finite duration requires the convolution of the delta-function pulse solution with the pulse shape itself. Therefore, given the solution to an infinitely narrow pulse, p_δ the solution of the finitely large pulse is given as

$$p(\boldsymbol{r},t)=\int_{-\infty}^{+\infty}dt' p_{\delta}(\boldsymbol{r},t-t')S(t') \tag{2}$$

where $S(t)$ is the temporal pulse profile.[12] Pulsed proton sources from syncrocyclotrons tend to have pulses on the order of μs in duration, which is not insignificant compared to the time taken by the sound to travel to a transducer some cm away (a transducer 7.5 cm away from the source will have a signal travel time of 50 μs). Therefore, delta function excitation assumptions are typically not valid for proton pulses in the range of tens of μs.

Equation 2 can be discritized for the purposes of dealing with digital signal. For brevity, let $D_{\delta i}$ be the discretized pressure vs. time signal of the ith element in the delta function simulation (with i ranging from 1 to 256, to best emulate the situation from Figure 1) for the remainder of this manuscript.

We perform the numerical convolution of a Gaussian pulse of variable pulse width with our detected acoustic pressure for all 256 sensor elements. We first begin by resampling/interpolating $D_{\delta i}$ to match the length of our discretized $S(t)$, the re-sampling process is described in detail in the appendix. The resulting waveform, $D_{\tau i}$, represents the pressure that the sensor would detect in the case that the initial pressure was deposited over a finite time interval corresponding to a Gaussian pulse with width τ. Then,

$$D_{\tau i}(k)=\sum_{j}D_{\delta i}(j)S(k-j+1) \tag{3}$$

where all functions are discretized. This can be turned into a function of time, $D_{\tau i}(t)$ by mapping the timestep vector to the elements within $D_{\tau i}(k)$.

It is important to note that equation 3 assumes that the transducer is a perfect broadband detector, thus idealized point detectors are considered for the remaining of the manuscript. If a more realistic detector is to be modelled accounting for potential bandwidth limitations of a transducer, then $D_{\tau i}$ must be filtered according to the transducer bandwidth. The simplest way to do this is to multiply by the transducer gain G(f) in frequency space.

The frequency of the protoacoustic signal is a crucial property for detection. So we will present here our derivations on how the pulse-width, shape, and transducer bandwidth is expected to influence the frequency spectrum of the generated signal. As real transducers are bandwidth limited, in experiment it is vital that the transducer bandwidth match the spectrum of the generated signal. For this we present a method through which the expected spectrum of generated systems can be modelled prior to experiment, for both triangle and Gaussian pulses.

An intuitive way to understand the entire signal detection process is in Fourier space, as the convolution operater is equal to multiplication in Fourier space. Focussing in a single detection element (a single transducer), here we outline the theory behind signal detection. Let the detected signal by the single element be P, then the Fourier transform of this signal, $\hat{P}$, is given by

$$\hat{P}(f) = \hat{S}(f)\hat{D}_{\delta}(f)G(f) \quad (4)$$

where D_{δ} is the temporal impulse response of this element (this is the signal that would be detected if the pulse duration was infinitely short), and S is the temporal profile of the pulse. Here, the ˆ accent denotes a Fourier transform, and f is the frequency. G is the frequency dependent gain function of the transducer. It should be noted that equation 4 consists first of the convolution operation in Fourier space (through the convolution theorem), followed by multiplication by the gain function of the transducer in Fourier space.

Through equation 4, all components of signal detection are incorporated into the final model. $\hat{D}_{\delta}(f)$ encodes information with regard to the geometry of the sample itself, $G(f)$ encodes the transducers frequency response, and $\hat{S}(f)$ incorporates the pulse width dependence of the signal. It is important for all protoacoustic experimental planning to consider all aspects of equation 4, as this equation can ultimately guide transducer choice, proton beam choice, and object choice.

In equation 4, the only pulse width dependent multiplicand is $\hat{S}(f)$. And therefore the frequency dependence of pulse can be well understood through this function. Fortunately, $\hat{S}(f)$ is simply the Fourier transform of the temporal pulse profile, so can be easily extracted either analytically or numerically from various pulse shapes. For Gaussian pulses, we have extracted the analytic form of $\hat{S}(f)$ for Triangle, Gaussian, and Trapezoidal pulses in the appendix.

B. Frequency impact on resolution

Ultimately the major governing factor in protoacoustic imaging resolution will be the highest detectable frequency in the final signal given in equation 4, which is the main topic of study in this paper. Here we present various analyses of the protoacoustic frequency and its relation to pulse shape and image quality. We begin by presenting a simulation workflow for protoacoustic imaging. We then deploy this workflow to analyze the impact that protoacoustic pulse width can have on 3D image quality. We also examine the impact of Signal-to-Noise ratio at single transducer elements on the final reconstructed image of the proton dose. Finally, we collect an experimentally detected $S(t)$ and contrast this with signals of comparable time duration but different pulse shape.

C. Monte Carlo Simulations

We design and deploy a 5 step simulation workflow in order to achieve realistic protoacoustic simulations in line with clinical parameters (Figure 2). The first step is to conduct a planning CT of the sample in question. For convenience, we have done with a 30 cm × 30 cm × 30 cm solid water phantom which is a homogenous target (the solid water phantom consists of 14 blocks of varying thickness from 1–4 cm, which is why there are some vertical heterogeneities in the CT as shown in Figure 3). This was done to obtain quality assurance (QA) measurements and then use the logfile to compensate for delivery uncertainties (spot MU, spot position and adaptive collimator positions). The CT is merged with a realistic human body structure set, featuring a prostate, rectum, and bladder and

their respective positions. A standard two fields spot scanning proton treatment plan was generated to target the prostate as the main tumor site (Field one: 13 layers/438 spots. Field two: 13 layers/456 spots. 2Gy/fraction. Maximum MU per spot: 8.2746 MU. Minimum MU per spot: 0.2612 MU). After the plan was delivered on a Mevion S250i proton system, the system logfile was then captured and converted into simulation ready text file with in house tools. [13].

With a completed beam line components model, a TOPAS Monte Carlo (MC) simulation was then run on the Water phantom corresponding to machine delivery parameters including real time spots positions, spot MU values and adpative apeture leaf positions. TOPAS is a toolkit to make advanced Monte Carlo simulation of all forms of radiotherapy easier to use for medical physicists by providing the means to model x-ray and particle therapy treatment heads, model a patient geometry based on CT images, score dose, fluence, etc. [14]

D. Co-registration

The TOPAS simulation was run on a small part of the water phantom with different spacing than the original CT. This is for the purpose of saving computation time. Therefore to run k-wave simulations on the resulting dose, the dose must be co-registered with the scouting CT prior to k-wave simulation. The k-wave MATLAB toolbox is an open source toolbox developed for time domain acoustic and ultrasound simulations in complex and tissue-realistic media. The dose output of the MC simulation was overlaid with the solid water phantom CT via feature based co-registration in 3D slicer [15], [16]. The result of the co-registration is shown in Figure 3. A 3D structure set of organs was overlaid on both the dose output of MC simulations and the 3D solid water phantom. The two images were then co-registered via the use of this common structure of prostate.

E. K-wave Forward Simulation

Following the MC simulations of the proton dose, the dose is imported into MATLAB using the function dicomread. Here, the 3D dose can be used as a 3D initial condition to equation 1 using the k-wave MATLAB toolbox [17], [18]. As the dose is linearly proportional to the protoacoustic initial pressure, this linearity be used to generate relative protoacoustic pressure maps in MATLAB. This simulation is modelling a delta function pulse in order to obtain an estimate of p_o. After initialization, the pressure is then allowed to propagate throughout the sample using a pseudospectral solution method. For speed, the code is run using the C++ version of k-wave as opposed to running the simulations in MATLAB.

It is important to note, however, that protoacoustic imaging of the Mevion S250i would not image the entire dose deposited, only individual shots of the proton beam. Therefore, for this machine, protoacoustic imaging can only image single shot dose deposition at once. However, the sum of images of all shots can be overlaid following proton emission, thereby allowing protoacoustic imaging to reconstruct the total dose deposited. In this paper, we proceed assuming that an equivilant procedure can be suitably modelled by simulating the cumulative dose as an full dose deposited at once. We believe that this is a valid assumption as the cumulative protoacoustic pressure of all shots will itself be proportional

to the cumulative dose, thus requiring only the addition of reconstruction pressure from only individual shots of a proton pencil beam.

A sensor array matching the dimensions of a parallel receiving transducer element is also added to the simulation in order to simulate signal reception by an ultrasound transducer array. The sensor array consists of a 5×5 cm planar array with 16 elements evenly spaced in each direction. These dimensions were chosen to match a planar array that we possess and are actively using in experiments. The sensor array was placed to match the plane at $z = -150$ mm and the center of the sample was set at z = 0 mm.

All the simulations performed throughout this manuscript are forward modelling of the initial value problem, governed by equation 1. The size of the input matrix used to generate the initial pressure changed depending on the experimental sampling or the actual theoretical simulation. The experimental simulation had a grid size due to sampling of 532×532×144 with exact grid spacing of dx ≈ 1.3 mm, dy ≈ 1.3 mm, and dz = 2.5 mm. The cfl number used on this simulation was the default for k-wave which is 0.3. As for the properties and simulation of the water medium, A density value of 1000 kg/m^3, A Grüneisen parameter of 0.86 and an energy conversion efficiency of 1 were implemented. Furthermore, an acoustic attenuation model was implemented through the k-wave package. The point sensors on the simulation were spread through the x and y axis leaving the z axis as the propagation direction.

F. Noise Analysis

White noise with maximun amplitude equivalent to the maximum point of the signal was generated using a random generating function. This noise was then added to the detected signal prior to reconstruction. The effect of varying Signal-to-Noise-Ratios (SNRs) on image reconstructiuon was investigated.

G. Reconstruction

The final step in the simulation workflow is the reconstruction of the dose via a time reversal algorithm, which is conveniently built into the k-wave toolbox. This is done through the reconstruction of the initial pressure in the k-wave simulation. After $D_{ri}(t)$ is obtained by convolution of a Gaussian pulse, the sensor positions in the simulation now have the boundary condition

$$P_i = D_{ri}(t)$$

in time can be enforced, where P_i is the pressure at the location of sensor i. The simulation is now run in reverse in time and the pressure is allowed to propagate.

One consideration that must be made is the avoidance of the inverse-crime in numerical reconstruction, in order to account for this fact the reverse simulation is performed with an increment of 5% in the number of grid points than the forward simulation [17], [19].

H. Quality of reconstruction

A quantitative metric to quantify the quality of the reconstruction is required to properly evaluate the success of the reconstruction. For this set of simulation experiments, the mean-squared difference between the initial pressure and the reconstruction at each point was used as the metric to evaluate the quality of the simulation. This was performed by the MATLAB function immse, which uses the following equation to calculate the square mean difference:

$$MSE = \frac{\sum(Initial\ \ Pressure - Reconstructed\ \ Pressure)^2}{Sample\ \ Size}$$

I. Single Dose Experiment

An experiment using a single dose shot was performed and used as input to create a simulation and reconstruction with 2D planar transducer array at different distances from the Bragg peak. This allows to explore the type and frequency that the transducers are going to detect at those locations. The transducers were spaced out on the lateral direction by 46 mm and in the axial direction by 50 mm.

J. Experimental Beam Intensity Signal Collection

Active proton pulse signals were monitored with a Beam Exit Quadrant Foil Chamber (BEQ) immediately placed at the exit port of cylcotron. A Faraday cup, built in house according to the design of Cascio and Gottschalk[20], together with a high speed current amplifier (HCA-4M-500K, FEMTO, Germany), was mounted on the gantry nozzle at vault isocenter to measured the single proton pulse width and charge.

III. Results

A. Forward Simulations and Reconstruction

In order to understand the spatial heating function, a forward simulation was carried out for a single spot dose in Figure 4. Here, some important characteristics of the spatial heating function can be visualized. This simulation consists of a spot dose (Figure 4a) along with some idealized transducers (unlimited bandwidth and perfect sensitivity). While transducer 1 (directly on the Bragg peak) does detect some frequencies in MHz, they quickly decay by the time the pulse arrives at transducer 2 (5 cm away). However, it can be seen upon close visual inspection of the waveform from transducer 2 that there is still a non-zero (albeit weak) contribution of a 1MHz signal at this distance from the beam.

Following on the spot dose simulation, we also ran protoacoustic simulations of the overall dose delivered (which would be the cumulative result of individual spot doses). This was for the purpose of examining the impact of the pulse width on the signal. Reconstructions were run for a variety of protoacoustic pulse widths, specically at τ = 1ns(totesttheconvolutionscript), 1μs, 10μs, 15μs, and 30μs. An example output (with τ = 1 μs) is show in Figure 5. It can be seen that at this pulse width, while there are some artifacts present, the pressure can be reconstructed with relatively good fidelity.

The performance of the reconstruction, as expected, decays with increasing pulse width. The pulse width dependence on the reconstruction is shown in Figure 6. As the timestep for the delta function simulation is only ~ 0.25μs, the simulation where τ = 1ns is exactly identical to the delta function reconstruction. Nevertheless we have chosen to include it in Figure 6 as it confirms to us that our numerical convolution script works as intended. It can be seen that at very low pulse widths the reconstruction performs best. This is because at these pulse widths, $\sum_j D_{\delta i}(j)S(k-j+1) \approx D_{\delta i}(k)$, and the convolution function does not change the characteristics of the signal all that much. This is consistent with what has been reported in literature [12], [21], [22].

Furthemore, the mean square difference (Table I) between the initial pressure and the reconstruction shown an increase with increasing pulse width. These results support the trend in Figure 6, where the performance and quality of the reconstruction decay with increasing pulse width.

The condition of stress confinement on pulse width is given as

$$\tau < d_c / v_S$$

where d_C is the desired resolution. As this simulation operates in a discretized space, the maximum achievable resolution in the simulation is limited by the grid spacing, which matches the dimensions of the planning CT scan (1.3 mm in x and y directions, 2.5 mm in the z direction). This corresponsed to a stress confinement time of 1.7 μs in water. Therefore, stress confinement at this length scale is met for all simulations of $\tau < 1.7\mu$s.

The effect of stress confinement can be seen in Figure 6. All the reconstructions that satisfy stress confinement ($\tau < 1.7\mu$s) look identical to one another. This is because all of these conditions are well appoximated as delta pulse excitations at the resolution limits set by the planning CTs. However, once stress confinement starts to be breached at the planning CT resolutions, resolution decay in the Bragg peak reconstruction is visible. These simulations demonstrate a useful guideline in clinical procedure of determining the optimal proton pulse width for the desired accuracy of Bragg peak localization. The dose deposited can also be rendered in 3D using rendering software such as AMIRA (rendering available in the appendix).

The effect of varying the SNR on signal reconstruction when $\tau = 15\mu$s can be seen in Figure 7, as expected poorer SNRs results in poorer reconstruction of the initial dose, with an SNR of 5 very accurately reproducing the initial pressure. However, it can be seen that even when the amplitude of noise is higher than the amplitude of the signal (SNR<1), the dose deposition can be partially made out, albeit with low resolution. The reason that the reconstruction algorithm can still reconstruct something despite the noise being stronger than the signal, is that the time-reveral procedure maps the detected signal at all transducers back towards the source. Therefore, across all transducers which now act as emitters during time reversal, there is an ‘averaging’ effect that occurs because noise from various transducers is send back into the sample geometry. As the noise from different transducers gets averaged out, some of the original dose still appears even with an SNR of

<1. This bodes well for experimental set-ups as it implies that, if SNR at a single element is <1, running the reconstruction algorithm may still reveal useful information about the dose distribution.

B. Pulse Shape Dependence of frequency

To examine the effect of pulse width on frequency, we consider an experimental $S(t)$ obtained from a clinical proton machine. Figure 8a shows the signal recorded with a BEQ chamber in low temporal resolution, with multiple pulses (spikes) present. At this level the overall pulsing behavior of the proton machine can be seen but individual pulses width cannot be accurately made out due to slow electronics. Figure 8b shows a zoomed in version of the pulses, recorded with a Faraday cup with a high speed Amp so as to show the pulse shape. It can be seen from Figure 8b that the shape of the beam is roughly that of a skewed Gaussian, as is also common in photoacoustic context. Therefore we have fit a Gaussian to the curve and taken its analytic Fourier Transform (derivation in appendix), shown in Figure 8c. Interesingly, it can be seen that the maximum frequency present in this signal is well in the range of MHz, yet μs pulses from clinical linear accelerators do not usually generate signals in the MHz range. This implies that the major roadblock for high frequency generation in proton-acoustics is more spatial than temporal, as a comparison between Figure 8 and Figure 4 shows that by far the bottleneck of low frequency is in the spatial heating function of the proton beam as opposed to the temporal pulse shape.

Figure 4, taken with the result from the spot dose, rein-forces that while pulse width is an important factor for thermoacoustic generation, it is not the only factor to consider. Ultimately the driving function in equation 1 is the derivative of the temperature rise. Therefore, a pulse with a sufficiently quick rise time, even if total duration is long, should also be able to generate thermoacoustic signals at higher frequencies. This is illustrated in the appendix (Figure 9), where a trapezoidal signal is examined with $4\mu s$ pulse duration and 125ns rise time. This signal shape is chosen to match those typically observed in clinical LINACs. It can be seen that the Fourier transform of such a pulse still contains significant frequency contributions in the MHz range, as is the case for a Gaussian μs pulse examined above. We have simulated the Gain function, $G(f)$, of a transducer with a flat passband of 1–4MHz, and it can be seen from the product of the $G(f)$ and $\hat{S}(f)$ that the final signal (prior to convolution with D_δ as in equation 4) has significant frequency contributions in the MHz range. Therefore, even signals with several μs duration can be engineered in such a way that they can generate high-frequency signals in the MHz range. Such frequency ranges are much more suitable for high-resolution protoacoustic imaging than those typically observed from clinical machines and so the spatial heating function again is the main bottleneck. Therefore, this work, combined with our results in Figure 6, implies that there is a distinct benefit in the contect of protoacoustic imaging towards making spatial gradients as sharp as possible in protoacoustic imaging (e.g. with some artificial absorber or contrast agent present), as this has the potential to yield much higher frequencies than are typically observed in thermoacoustic clinical experiments.

It additionally implies that whereas historically it has been assumed that clinical radiation sources with μs pulse durations will only generate frequencies in the kHz range, it is

possible to generate MHz signals from μs pulses as well if the spatial gradients from the beam are sufficiently sharp. An interesting consequence of this exercise is that we have a plausible explanation for why μs pulse trains, as are common in conventional x-ray LINACs, may actually generate thermoacoustic signals that are of higher frequency than expected. Essentially, as LINACs use a pulse train with a trapezoidal envelope, the most rapid change in S(t) occurs at the rise and fall, therefore a trapezoidal signal with rise time in the range of ns can in theory produce a thermoacoustic signal that is in the MHz range. This can serve to explain why other studies [23] have observed signals in the MHz range despite using beams with pulse durations in the range of several μs. The underlying implication of this is that if the rise time of a source is sufficiently sharp then this can potentially produce high frequency signals even if the total pulse duration is longer

Our theoretical analysis of the proton frequency can provide a road map to clinicians interested in conducting protoacoustic experiments. A crucial experimental consideration in thermoacoustics is the expected frequency spectrum of the detected signal. This is a key factor in choosing appropriate detection equipment with appropriate bandwidth. Using our workflow, protoacoustic experiments can be planned such that the bandwidths of detecting transducer overlaps well with the frequencies present in the signal, incorporating both the geometric characteristics of the sample as well as the temporal characteristics of the radiation excitation.

IV. Discussion

A. Simulation output

The simulation workflow demonstrated in this study provides a road-map through which clinicians can assess the feasibility of protoacoustic range verification for a wide variety of proton Bragg peaks. The simulation workflow is versatile with the planning CT used, the pulse width of the generated proton beam, the detector distribution, the size of the simulation region, and sound speed. While we have not done so here, this reconstruction is also robust to heterogeneities in sound speed in the sample, as the time reversed simulation is run with the same grid that ran the forward simulation, therefore if the planning CT can map tissue sound speeds and densities, this is a usable workflow for clinical practice.

We have also showed that reconstruction of the dose is possible even in the situation where individual element SNR is <1, due to the averaging effects of the time-reversal algorithm. This is particularly interesting from an experimental standpoint as it implies that imaging with an array and reconstructing can benefit from unique advantages of time reversal ‘averaging’ effects. That being said, single pulse measurements will almost certainly not be detectable with SNR <1, and will require many averages as is typical in protoacoustic experiments to achieve SNR>1 in a single element. Therefore, it is crucially important to emphasize that while ‘averaging’ effects from time reversal enable some image reconstruction when single element signals are <1, it will still likely be important to perform multiple averages over single elements.

Our simulation results show that protoacoustic Bragg peak localization is possible in 3D with a 2D matrix ultrasound array, and therefore that full relative dose reconstruction (i.e.

an image where the brightest pixel is the maximum initial pressure) is possible using protoacoustic Bragg peak range verification.

We have simulated 3D dose map of the proton beam with protoacoustic imaging with a 2D matrix ultrasound array. This can overcome the challenge of using a point-detector which requires raster scanning to generate images. Theoretically, the Bragg peak can not be localized with single acoustic detector. To pinpoint the exact localize of the point protoacoustic source, a minimal of three detecotors is needed. For high-resolution clinical imaging however, many more detectors are needed.

Additionally, the speed of the simulation can be improved upon via the use of parallel processing techniques. Currently our forward and reverse simulations run on a conventional dual core desktop computer, which can limit the time of the simulations to several hours. However, through parallelization of the Fourier transform step used in k-wave's pseudospectral method, the speed of simulations can be drastically improved roughly linearly with the number of cores available.

With regard to desired frequency, current accepted range uncertainty for measuring the Bragg peak is typically 1 mm. However in clinical situations this can increase to 1 mm+3.5 % of the proton range. These desired resolutions correspond to protoacousitc signal frequencies of kHz being acceptable. However, it should be noted that the acceptable uncertainty is itself partially determined by the accuracy of measurments, so if protoacoustic measurments can enable more accurate range measurments then we hope that this could reduce the maximal Bragg peak uncertainty in both measured and clinical cases.

B. Limitations

There are some important limitations of this approach that should be mentioned. Specifically, the simulation only uses point sensors and so does not simulate the effect of sensors themselves having some size. The simulation also assumes a uniform water medium, which can approximate tissue but is not the same as using soft tissue medium which could change propagation parameters. Addtionally, unlike van Dongen *et al.* [8], we have not considered heterogeneities in this study. We believe that a combination approach which considers 3D tissue heterogeneities while simultaneously using clinical logfiles on heterogeneous tissue phantoms would be the most accurate possible way to conduct protoacoustic simulations and propose this as a goal for future study. We also note that we have not explicitly modelled the impact of transducer bandwidth on the final reconstruction, and have assumed perfect bandwidth. This so that the impact of the pulse width could be analyzed independently, though future studies can perform a similar study on bandwidth by bandpass filtering prior to time reversal reconstruction.

It should also be noted that the reconstruction accuracy can be affected if acoustic properties of the sample change change (due to breathing) and heterogeneities play a large role in signal scattering. Therefore ideal deployment of this method would be either coupled with patient breath hold or deployed in areas that are mostly static during patient breathing.

We also note that the ideal modelling of this scenario would be that of thousands of spot doses which we would then reconstruct individually and then combine at the end. However there are several reasons we elected to instead use the cumulative dose in lieu of the individual spot doses. Firstly, the proton spot dose frequency spectrum (Figure 4) is determined primarily by the sharpness of the Bragg peak, which (except for very low energies) is on the order of mm. This Bragg peak sharpness means that the spatial gradients expected are at comparable length scaled to those of the cumulative dose, and so we concluded that frequency modelling would not be a major problem in performing out simulations this way. Secondly, the cumulative dose gradient was not as sharp as the Bragg peak dose gradient, so we could be assured that our simulations are not overly optimistic with imaging resolution. Lastly, running thousands of spot doses reconstructions was very computationally expensive in both processing and memory requirements, and so we elected to run simulations modelling the cumulative dose in lieu of many spot doses.

V. Conclusion

In conclusion, we have demonstrated here a function workflow for 3D protoacoustic imaging with the input of real clinical treatment record. For the first time, we have done these using MC simulations that utilize real delivered treatment machine records rather than only using treatment plan parameters. The simulation workflow is robust to sample geometries and sensor geometries and can serve as a useful tool for investigations of the feasibility of proton therapy on a wide variety of proton machines for which the temporal radiation pulse profile is well known.

We have shown that dose reconstruction is possible in protoacoustics using an array even if the SNR of all individual elements is <1, which implies that protoacoustic imaging may be more sensitive than previously thought as time reversal reconstruction can introduce an ‘averaging’ effect as noisy signals are time-reversed into the simulation geometry.

We have also shown that it is possible to generate high frequency signals from longer pulses if the rise time of the pulses is sufficiently sharp (so long as the spatial distribution of the beam has sufficiently sharp gradients). This provides an explanation of previous experiments where such phenomena was observed experimentally with x-ray beams [23]. Our work here demonstrates the importance of future proton machines to try and maximize spatial heat gradients and minimize pulse width for the sake of protoacoustic imaging, as a strong signal from a proton source can be used to enable image guidance. Additionally, we have provided an explanation for why in certain conditions, beams with large pulse durations on the order of several μs can generate MHz acoustic signals [23].

We believe that protoacoustic imaging can enable 3D, high-resolution, real-time mapping of proton dose during radiation therapy. Through the workflow demonstrated here, researchers can conveniently model protoacoustic imaging and enable further development of this technology towards clinical application.

Acknowledgments

This work did not involve human subjects or animals in its research. This work was supported by the National Institute of Health (R37CA240806), American Cancer Society (133697-RSG-19-110-01-CCE). The authors would like to acknowledge the support from UCI Chao Family Comprehensive Cancer Center (P30CA062203).

VII.: Appendix: Re-Sampling of $D_{\delta i}$ For Convolution

In order to enable convolution between p_δ and $S(t)$, both must first be discretized and matched in sampling rates to enable accurate convolution output. In the case of p_δ, discritization is automatic as the recorded pressures on all of the sensor elements are themselves vectors representing pressure as a discritized function of time, with timestep dt. The continuous form of a Gaussian $S(t)$ is modelled as

$$S(t) = \mathrm{Exp}\left(-4\ln 2\left(\frac{t}{\tau}\right)^2\right)$$

where τ is the pulse width. We discretize $S(t)$ using the sampling interval from -5τ to 5τ with sampling interval of $\frac{\tau}{20}$. For accurate convolution, $D_{\delta i}$ must also be re-sampled to match this sampling interval. We perform this in MATLAB using the function interp1. We then perform the convolution function and then downsample the resulting $D_{\tau i}$ back to the sampling rate of $D_{\delta i}$. This re-sampling allows for speed in the time-reversal simulation while at the same time enabling accurate convolution for incorporating pulse width into our simulation.

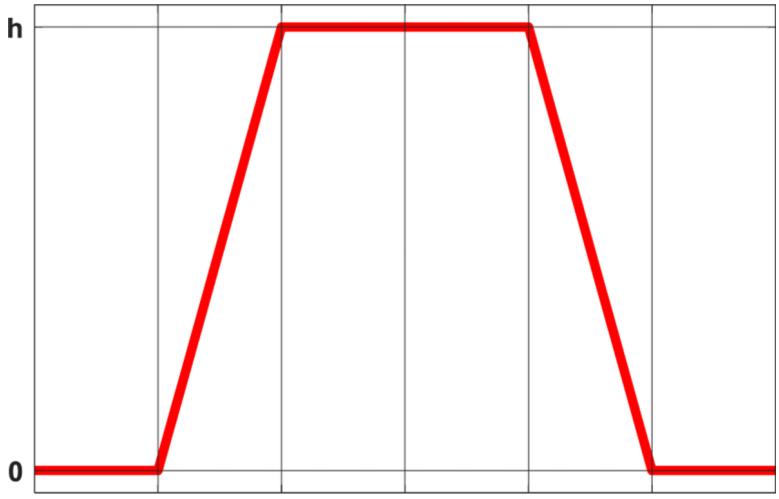

Fig. 9.
Trapezoidal Pulse waveform

VIII.: Appendix: Derivation of Analytic Fourier Transform for Gaussian, Triangle, and Trapezoidal Pulses.

The Gaussian Fourier transform is the simplest to derive, for a Gaussian pulse of the form $S(t) = Ae^{-\frac{t^2}{\tau^2}}$, the Fourier transform is

$$\hat{S}(f) = F\left[Ae^{-\frac{t^2}{\tau^2}}\right] = \int_{-\infty}^{\infty} Ae^{-\frac{t^2}{\tau^2}} e^{-2\pi i f t} \mathrm{d}t = \sqrt{\pi} A\tau e^{-\pi^2 \tau^2 f^2}$$

This represents the expected frequencies inherent in the detected signal, prior to convolution with the temporal impulse response. The Full width at half maximum

For a triangle pulse, a similar process can be done, the trigangle function with pulse width τ is given as

$$S(t) = \begin{cases} 1 - \frac{2}{\tau}\left|t\right| & \text{if } \left|t\right| \leq \frac{\tau}{2}, \\ 0 & \text{otherwise} \end{cases}$$

The Fourier transform can be taken similarly

$$\check{S}(f) = \int_{-\frac{\tau}{2}}^{0} \left(1 + \frac{2t}{\tau}\right) e^{-2\pi i f t} \mathrm{d}t + \int_{0}^{-\frac{\tau}{2}} \left(1 - \frac{2t}{\tau}\right) e^{-2\pi i f t} \mathrm{d}t$$

$$\check{S}(f) = \frac{2\sin^2(\pi f \theta_{RT})}{\pi^2 f^2 \theta_{RT}} \tag{5}$$

This is a periodic function with roots at $f = \frac{2n}{\tau}, n \in \mathbb{Z}$, and local maxima located directly between roots detected by a transducer.

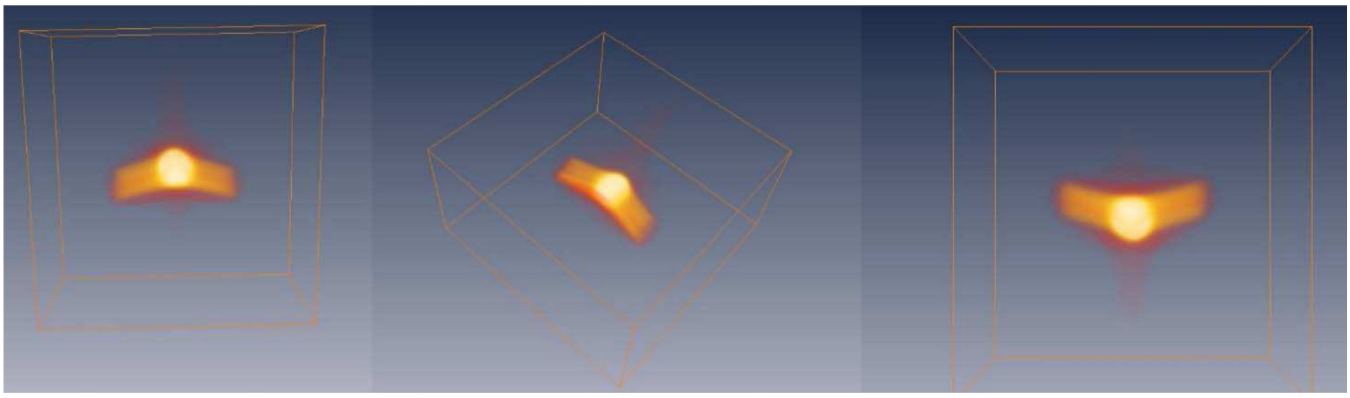

Fig. 10.
3D rendering of dose reconstruction with $\tau = 1\mu$s, the reconstruction matches the treatment plan well.

For a trapezoidal pulse, we can model a trapezoid with some top width $2W$, rise time T_r, and height h with the equation

$$S(t) = \begin{cases} b - \frac{h}{T_r}|t| & \text{if } W \le |t| \le W + T_r, \\ h & \text{if } |t| < W \\ 0 & otherwise \end{cases}$$

where $b = \frac{hW}{T_R} + h$. This is shown above in Figure 9. To evaluate the Fourier transform, we split the function up into its pieces and integrate the non-zero portions as follows

$$\breve{S}(f) = \int_{-W-T_r}^{-W} \left(b + \frac{h}{T_r}t\right) e^{-2\pi i f t} \mathrm{d}t + \int_{-W}^{W} h e^{-2\pi i f t} \mathrm{d}t + \int_{W}^{W+T_r} \left(b - \frac{h}{T_r}t\right) e^{-2\pi i f t} \mathrm{d}t$$

Solving this integral and simplifying yields

$$\breve{S}(f) = \frac{h \mathrm{Sin}[f\pi T] \mathrm{Sin}[f\pi(T + 2W)]}{f^2 \pi^2 T}$$

Which has zeros at $f = n/T$ and at $f = \frac{n}{T + 2W}$

IX.: Appendix: Three angles of a 3D rendered Dose for the 1 μs pulse duration

A three-dimensional rendered plot (Figure 10) was done for the dose at a pulse duration of 1 μs where different angles were portrait

X.: Derivation of Analytic Fourier Transform from Figure 8

The fit function of the Gaussian was $a \exp\left(-\frac{t-b}{c}\right)^2$ a, b, and c were fit parameters. Using the curve fitting tool on MATLAB yielded a fit with parameters a = 0.684, n = 4.65μs and c = 1.21 μs. As the horizontal position and the amplitude of the Gaussian were not important for frequency determination via the Fourier transform, we set $a = 1$ and $b = 0$. Taking the Fourier transform of the resulting Gaussian using the equations from section VII yields

$$\check{S}(f) = \sqrt{\pi}c\exp\left(-\pi^2 c^2 f^2\right).$$

References

[1]. Ahmad M, Xiang L, Yousefi S, and Xing L, "Theoretical detection threshold of the proton-acoustic range verification technique," Medical Physics, vol. 42, no. 10, pp. 5735–5744, 2015, doi: 10.1118/1.4929939. [PubMed: 26429247]

[2]. Kipergil EA, Erkol H, Kaya S, Gulsen G, and Unlu MB, "An analysis of beam parameters on proton-acoustic waves through an analytic approach," Phys. Med. Biol, vol. 62, no. 12, pp. 4694–4710, May 2017, doi: 10.1088/1361-6560/aa642c. [PubMed: 28252450]

[3]. Assmann W. et al. , "Ionoacoustic characterization of the proton Bragg peak with submillimeter accuracy," Medical Physics, vol. 42, no. 2, pp. 567–574, 2015, doi: 10.1118/1.4905047. [PubMed: 25652477]

[4]. Jones KC et al. , "Experimental observation of acoustic emissions generated by a pulsed proton beam from a hospital-based clinical cyclotron," Medical Physics, vol. 42, no. 12, pp. 7090–7097, 2015, doi: 10.1118/1.4935865. [PubMed: 26632062]

[5]. Samant P, Trevisi L, Ji X, and Xiang L, "X-ray induced acoustic computed tomography," Photoacoustics, vol. 19, p. 100177, Sep. 2020, doi: 10.1016/j.pacs.2020.100177.

[6]. Otero J, Felis I, Ardid M, and Herrero A, "Acoustic Localization of Bragg Peak Proton Beams for Hadrontherapy Monitoring," Sensors, vol. 19, no. 9, Art. no. 9, Jan. 2019, doi: 10.3390/s19091971.

[7]. Nie W, Jones KC, Petro S, Kassaee A, Sehgal CM, and Avery S, "Proton range verification in homogeneous materials through acoustic measurements," Phys. Med. Biol, vol. 63, no. 2, p. 025036, Jan. 2018, doi: 10.1088/1361-6560/aa9c1f.

[8]. van Dongen KWA, de Blécourt AJ, Lens E, Schaart DR, and Vos FM, "Reconstructing 3D proton dose distribution using ionoacoustics," Phys Med Biol, vol. 64, no. 22, p. 225005, Nov. 2019, doi: 10.1088/1361-6560/ab4cd5.

[9]. Jones KC, Witztum A, Sehgal CM, and Avery S, "Proton beam characterization by proton-induced acoustic emission: simulation studies," Phys Med Biol, vol. 59, no. 21, pp. 6549–6563, Nov. 2014, doi: 10.1088/0031-9155/59/21/6549. [PubMed: 25322212]

[10]. Yu Y, Li Z, Zhang D, Xing L, and Peng H, "Simulation studies of time reversal-based protoacoustic reconstruction for range and dose verification in proton therapy," Medical Physics, vol. 46, no. 8, pp. 3649–3662, 2019, doi: 10.1002/mp.13661. [PubMed: 31199511]

[11]. Wang LV, "Tutorial on Photoacoustic Microscopy and Computed Tomography," IEEE Journal of Selected Topics in Quantum Electronics, vol. 14, no. 1, pp. 171–179, Jan. 2008, doi: 10.1109/JSTQE.2007.913398.

[12]. Zhou Y, Yao J, and Wang LV, "Tutorial on photoacoustic tomography," J. Biomed. Opt, vol. 21, no. 6, pp. 061007–061007, 2016, doi: 10.1117/1.JBO.21.6.061007.

[13]. Chiang B-H, Bunker A, Jin H, Ahmad S, and Chen Y, "Developing a Monte Carlo model for MEVION S250i with HYPER-SCAN and Adaptive ApertureTM pencil beam scanning proton therapy system," Journal of Radiotherapy in Practice, pp. 1–8, 2020, doi:10.1017/S1460396920000266.

[14]. Perl J, Shin J, Schumann J, Faddegon B, and Paganetti H, "TOPAS: an innovative proton Monte Carlo platform for research and clinical applications," Med Phys, vol. 39, no. 11, pp. 6818–6837, Nov. 2012, doi: 10.1118/1.4758060. [PubMed: 23127075]

[15]. Muller L, Prusator M, Ahmad S, and Chen Y, "A complete workflow for utilizing Monte Carlo toolkits in clinical cases for a double-scattering proton therapy system," Journal of Applied Clinical Medical Physics, vol. 20, no. 1, pp. 23–30, 2019, doi: 10.1002/acm2.12473.

[16]. Kikinis R, Pieper SD, and Vosburgh KG, "3D Slicer: A Platform for Subject-Specific Image Analysis, Visualization, and Clinical Support," in Intraoperative Imaging and Image-Guided Therapy, Jolesz FA, Ed. New York, NY: Springer, 2014, pp. 277–289. doi: 10.1007/978-1-46147657-3_19.

[17]. Treeby BE and Cox BT, "k-Wave: MATLAB toolbox for the simulation and reconstruction of photoacoustic wave fields," J Biomed Opt, vol. 15, no. 2, p. 021314, Apr. 2010, doi: 10.1117/1.3360308.

[18]. Treeby BE, Jaros J, Rendell AP, and Cox BT, "Modeling nonlinear ultrasound propagation in heterogeneous media with power law absorption using a k-space pseudospectral method," J. Acoust. Soc. Am, vol. 131, no. 6, pp. 4324–4336, Jun. 2012, doi: 10.1121/1.4712021. [PubMed: 22712907]

[19]. Treeby BE, Jaros J, Rohrbach D, and Cox BT, "Modelling elastic wave propagation using the k-Wave MATLAB Toolbox," in 2014 IEEE International Ultrasonics Symposium, Sep. 2014, pp. 146–149. doi: 10.1109/ULTSYM.2014.0037.

[20]. Cascio EW and Gottschalk B, "A Simplified Vacuumless Faraday Cup for the Experimental Beamline at the Francis H. Burr Proton Therapy Center," in 2009 IEEE Radiation Effects Data Workshop, Jul. 2009, pp. 161–165. doi: 10.1109/REDW.2009.5336294.

[21]. Yao J. and Wang LV, "Sensitivity of photoacoustic microscopy," Photoacoustics, vol. 2, no. 2, pp. 87–101, Jun. 2014, doi: 10.1016/j.pacs.2014.04.002. [PubMed: 25302158]

[22]. Yao J. and Wang LV, "Photoacoustic Microscopy," Laser Photon Rev, vol. 7, no. 5, Sep. 2013, doi: 10.1002/lpor.201200060.

[23]. Lei Hao, "Developments and Applications of Laser-Based and X-Ray-Based Biomedical Thermoacoustic Imaging Techniques," 2019. Accessed: Dec. 04, 2020. [Online]. Available: https://deepblue.lib.umich.edu/handle/2027.42/150038

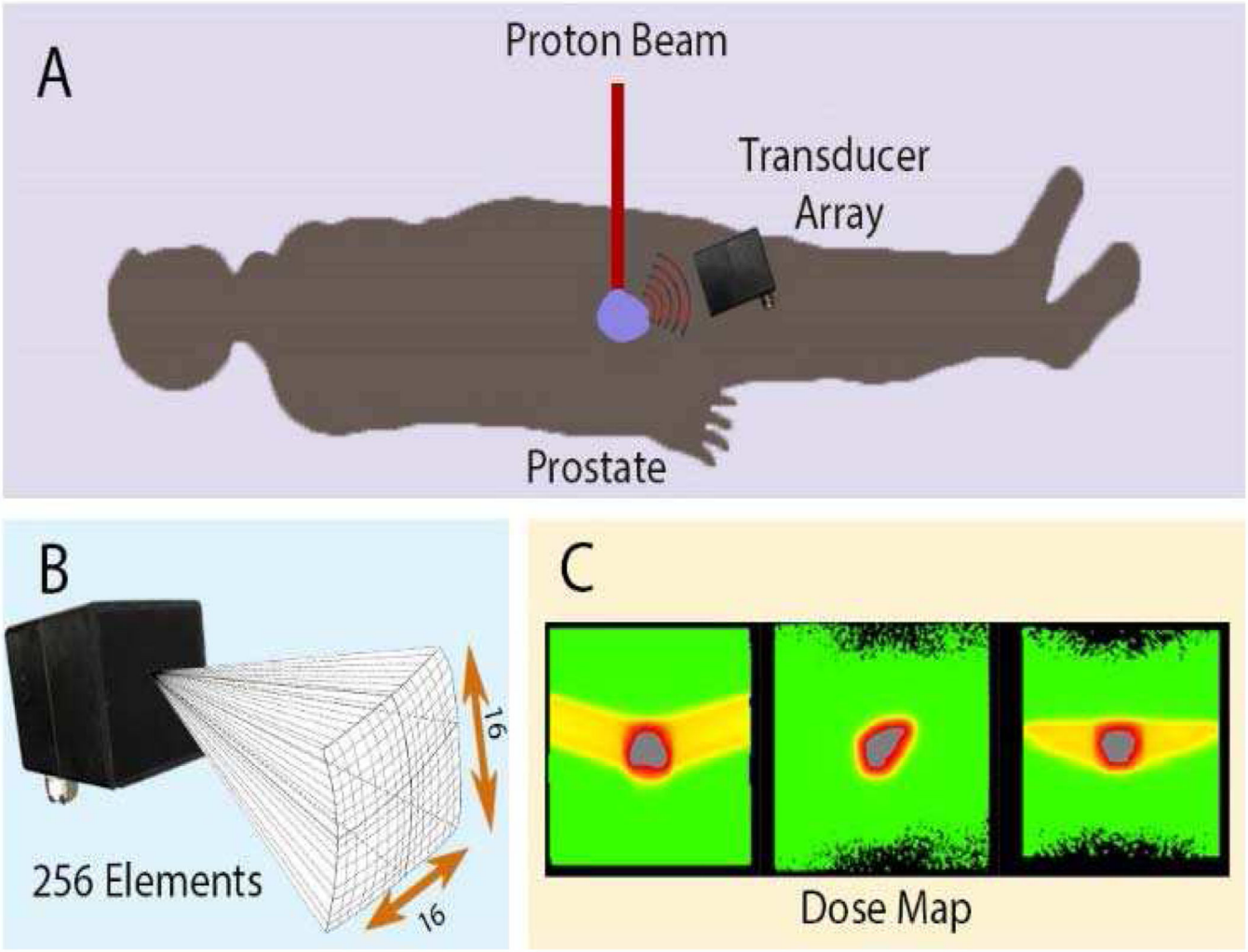

Fig. 1.

A) Protoacoustic dose imaging schematic diagram, a transperineal ultrasound transducer array captures a protoacoustic signal induced on the prostate b) zoomed in profile of the transducer, we simulate 256 transducers arranged in a 16 × 16 square grid c) an example of a dose map that could be reconstructed with this method, deposition dose is linearly proportional to the protoacoustic signal assuming a constant Grueneisen parameter.

Fig. 2.
Simulation Workflow for Protoacoustic Imaging

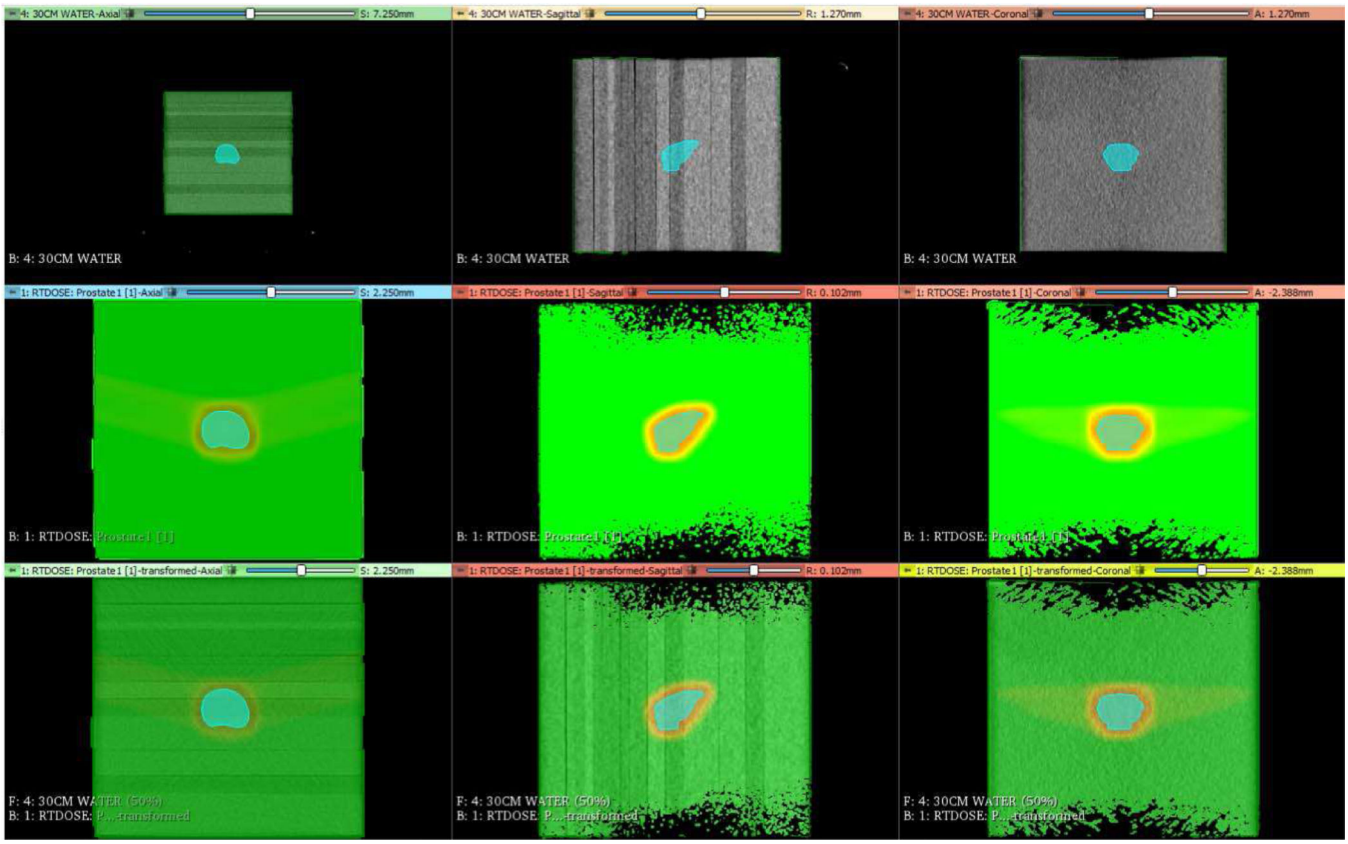

Fig. 3.

Co-Registration of CT image with MC dose plan. Top row: Phantom CT overlaid with digital prostate phantom (blue), Middle row: Proton Dose overlaid with digital prostate phantom (blue), Bottom row: Co-registered image with Phantom CT and prostate dose using feature mapping of the digital prostate phantom. Columns are the Axial, Sagittal, and Coronal plane views, from left to right, respectively.

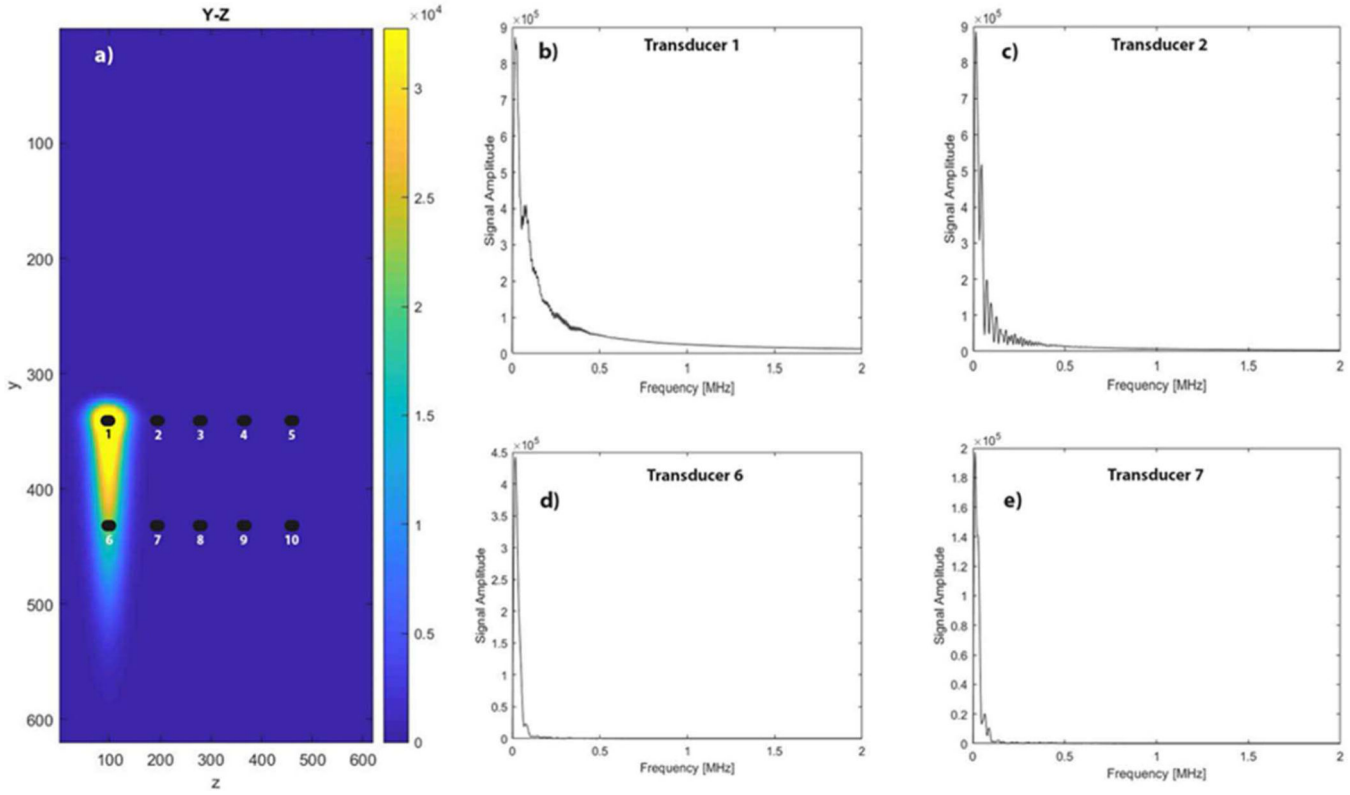

Fig. 4.

Single Dose Shot experiment with transducers at different positions. a) initial pressure with transducer location, b) tranducer 1 FFT, c) transducer 2 FFT, d) transducer 6 FFT, e) Transducer 7 FFT. All units are a.u.

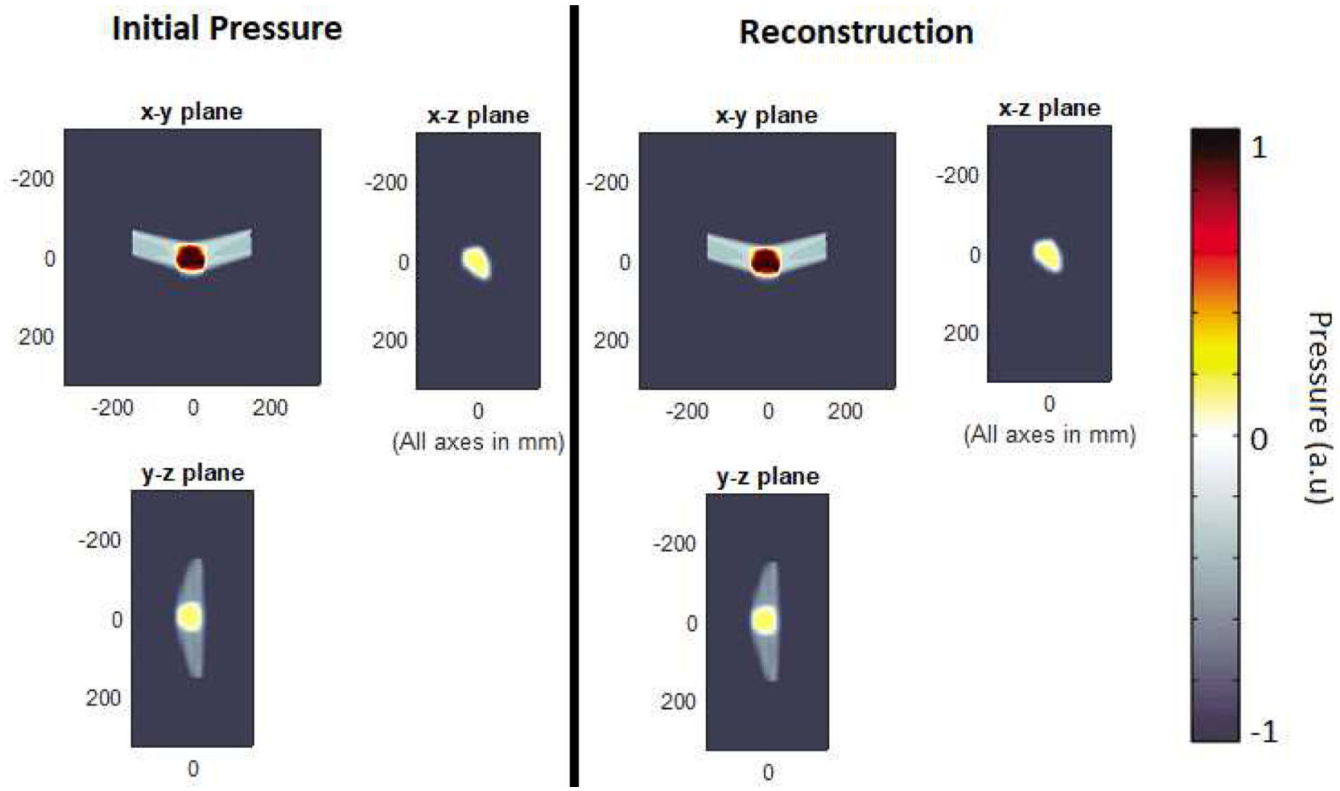

Fig. 5.

Initial (left) and Reconstructed (right) Pressures for a simulated proton source with $\tau = 1$ μs in three imaging planes xy, xz, yz shows the reconstruction of the initial pressure with relatively good fidelity in the range of stress confinement at CT resolutions. The artifices generated on the reconstruction can be better appreciated on subsequent figures.

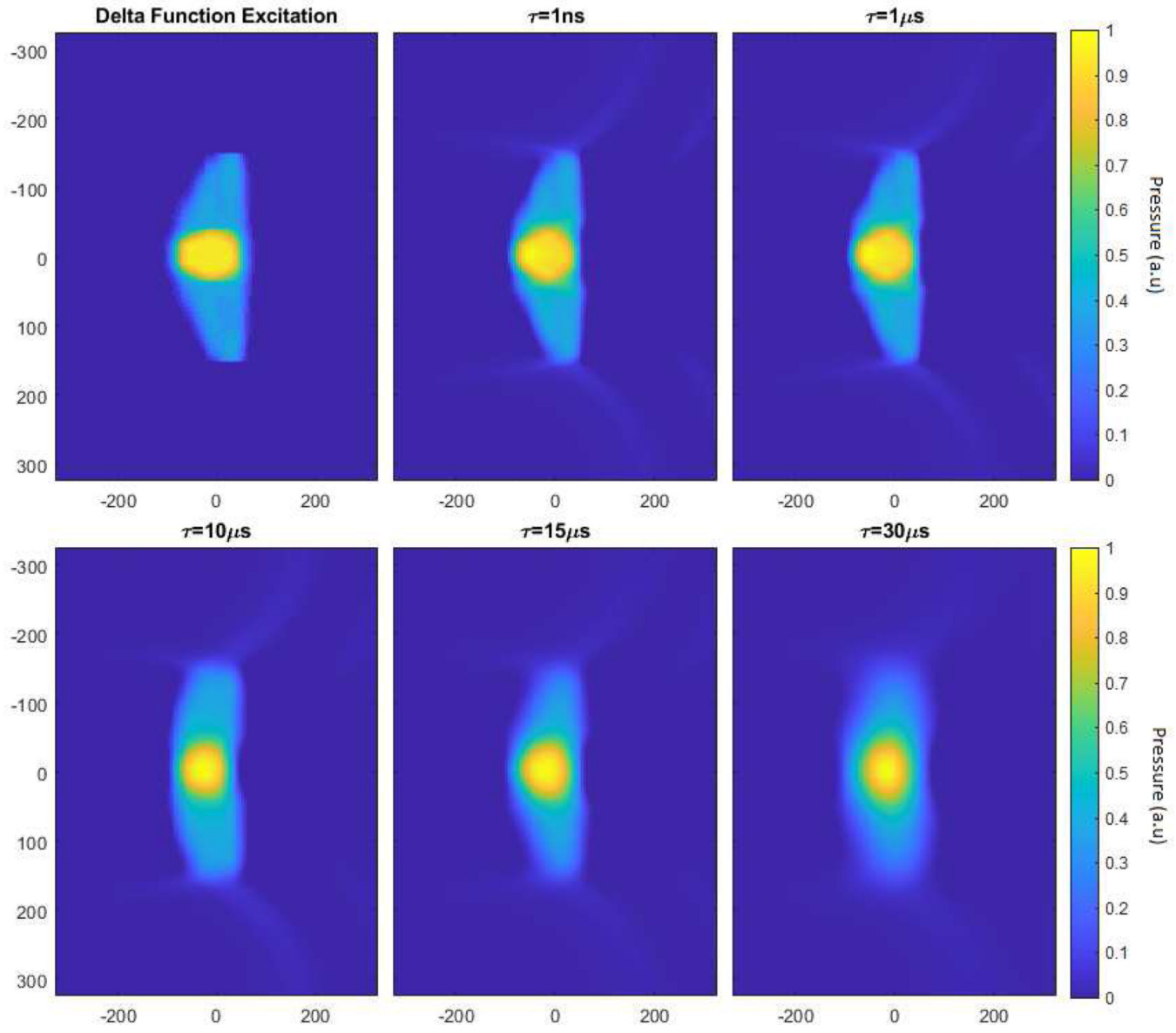

Fig. 6.

Pulse width dependence on Bragg peak Localization. All axes in mm (labels correspond to the z axis). Image colormap is normalized for all images Stress confinement occurs at $\tau < 1.7\mu$s. Planar detector array is at z = −150

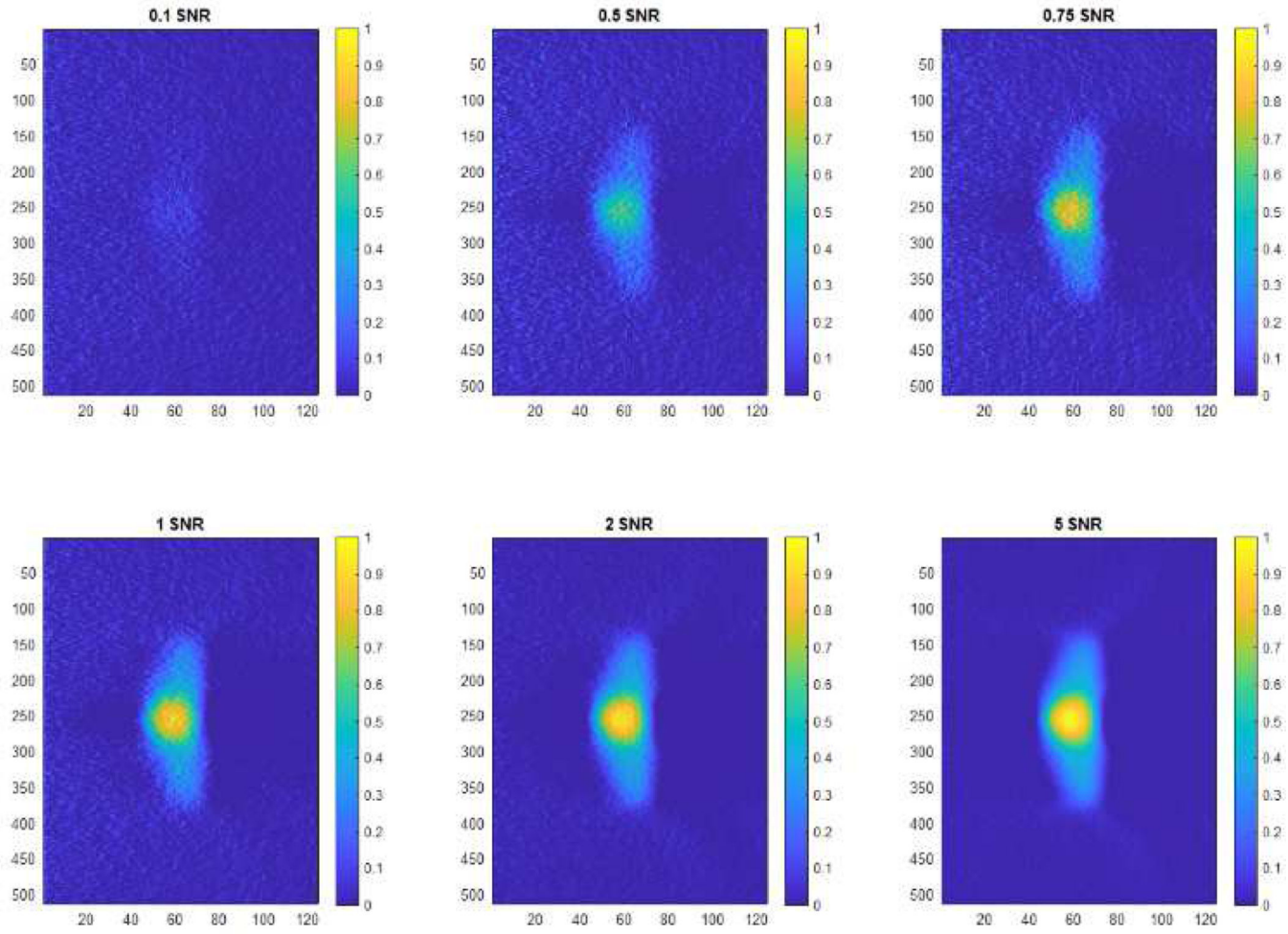

Fig. 7.

Effect of SNR on image reconstruction for a pulse with of 15 μs. Some reconstruction is possible even if the signal on individual transducer elements has SNR<1 due to the averaging effects of the time-reversal reconstruction algorithm. All axes in mm. Colourmap normalized in all cases.

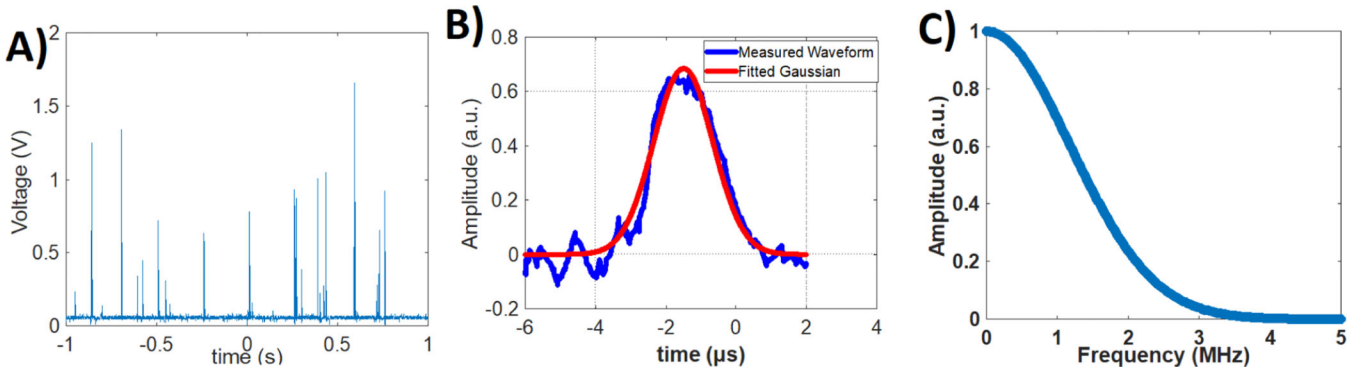

Fig. 8.

a) Intensity vs time of clinical proton machine, pulses can be seen as spikes. b) zoomed in waveform of a single pulse from a, pulse duration is several μs. Pulse shape reveals that the rise and fall are roughly a skewed Gaussian that can be fitted c) Fourier transform (power spectrum) of Gaussian fitted in b

TABLE I

MEAN SQUARE DIFFERENCES BETWEEN THE INITIAL PRESSURE AND THE RECONSTRUCTION

	Mean Square Difference
1nsPulse	2.60E-04
1usPulse	2.60E-04
10usPulse	2.97E-04
15usPulse	3.32E-04
30usPulse	6.46E-04